Chapter 9
Weak Focusing Synchrotron

Abstract This Chapter introduces to the weak focusing synchrotron, and to the theoretical material needed for the simulation exercises. It begins with a brief reminder of the historical context, and continues with beam optics and acceleration techniques which the weak synchrotron principle and methods lean on. Regarding the latter, it relies on basic charged particle optics and acceleration concepts introduced in the previous Chapters, and further addresses the following aspects:
- fixed closed orbit,
- periodic structure,
- periodic motion stability,
- optical functions,
- synchrotron motion,
- depolarizing resonances.

The simulation of weak synchrotrons only require a very limited number of optical elements; actually two are enough: DIPOLE or BEND to simulate combined function dipoles, and DRIFT to simulate straight section. A third one CAVITE, is required for acceleration. Particle monitoring requires keywords introduced in the previous Chapters, including FAISCEAU, FAISTORE, possibly PICKUPS, and some others. Spin motion computation and monitoring resort to SPNTRK, SPNPRT, FAISTORE. Optics matching and optimization use FIT[2]. SYSTEM again is used to shorten the input data files.

Notations used in the Text

B; $\mathbf{B}$, $B_{x,y,s}$	field value; field vector, its components in the moving frame
$B\rho = p/q$; $B\rho_0$	particle rigidity; reference rigidity
C; C_0	orbit length, $C = 2\pi R + \left[\begin{smallmatrix}\text{straight}\\ \text{sections}\end{smallmatrix}\right.$; reference, $C_0 = C(p = p_0)$
E	particle energy
EFB	Effective Field Boundary
f_{rev}, f_{rf}	revolution and accelerating voltage frequencies
h	RF harmonic number, $h = f_{\text{rf}}/f_{\text{rev}}$
m; m_0; M	mass, $m = \gamma m_0$; rest mass; in units of MeV/c^2
$n = \frac{\rho}{B}\frac{dB}{d\rho}$	focusing index
$\mathbf{p}$; p; p_0	momentum vector; its modulus; reference
$P_i,\ P_f$	polarization, initial, final
q	particle charge
$r,\ R$	orbital radius ; average radius, $R = C/2\pi$
s	path variable
v	particle velocity
$V(t)$; $\hat{V}$	oscillating voltage; its peak value
x, x', y, y'	horizontal and vertical coordinates in the moving frame

α	momentum compaction, or trajectory deviation
$\beta = v/c$; β_0; β_s	normalized particle velocity; reference; synchronous
β_u	betatron functions ($u:\ x, y, Y, Z$)
$\gamma = E/m_0$	Lorentz relativistic factor
Δp, δp	momentum offset
ε	wedge angle
ε_u	Courant-Snyder invariant ($u:\ x, r, y, l, Y, Z, s$, etc.)
ϵ_R	strength of a depolarizing resonance
μ_{u}	betatron phase advance, $\mu_{\text{u}} = \int_{\text{period}} ds/\beta_u(s)$ ($u:\ x, y, Y, Z$)
ν_{u}	wave number, radial, vertical, synchrotron ($u:\ x, y, Y, Z, l$)
ρ	curvature radius
ϕ; ϕ_s	particle phase at voltage gap; synchronous phase
ϕ_u	betatron phase advance, $\phi_u = \int ds/\beta_u$ ($u:\ x, y, Y, orZ$)
φ	spin angle to the vertical axis

Introduction

The synchrotron is an outcome of the mid-1940s longitudinal phase focusing synchronous acceleration concept [1, 2]. In its early version, transverse beam stability in the synchrotron during the thousands of turns that the acceleration lasts was based on the technique known at the time: weak focusing, as in the cyclotron and in the betatron. An existing betatron was used to first demonstrate phase-stable synchronous acceleration with slow vaiation of the magnetice field, on a fixed orbit, in 1946 [3], - closely following the demonstration of the principle of phase focusing using a fixed-field cyclotron [4].

Phase focusing states that stability of the longitudinal motion, longitudinal focusing, is obtained if particles in a bunch, which have a natural energy spread, arrive at the accelerating gap in the vicinity of a proper phase of the oscillating voltage, the synchronous phase; if this conditon is fullfilled the bunch stays together, in the vicinity of the latter, during accceleration. Synchrotrons operate in general in a non-isochronous regime: the revolution period changes with energy; as a consequence, in order to maintain an accelerated bunch on the synchronous phase, the RF voltage frequency, which satisfies $f_{\rm rf} = hf_{\rm rev}$, has to change continuously from injection to top energy. The reference orbit in a synchrotron is maintained at constant radius by ramping the guiding field in the main dipoles in synchronism with the acceleration, as in the betatron [5].

The synchrotron concept allowed the highest energy reach by particle accelerators at the time, it led to the construction of a series of proton rings with increasing energy: 1 GeV at Birmingham (1953), 3.3 GeV at the Cosmotron (Brookhaven National Laboratory, 1953-1969), 6.2 GeV at the Bevatron (Berkeley, 1954-1993), 10 GeV at the Synchro-Phasotron (JINR, Dubna, 1957-2003), and a few additional ones in the late 1950s well into the era of the concept which would essentially dethrone the weak focusing method and its quite bulky rings of magnets which were a practical limit to further increase in energy[1]: the strong focusing synchrotron (the object of Chapter 10). The general layout of these first weak focusing synchrotrons included straight sections (often 4, Fig. 9.1), which allowed insertion of injection (Fig. 9.1) and extraction systems, accelerating cavities, orbit correction and beam monitoring equipment.

The next decades following the invention of the synchrotron saw applications in many fields of science including fixed-target nuclear physics for particle discovery, material science, medicine, industry. Its technological simplicity still makes it an appropriate technology today in low energy beam application when relatively low current is not a concern, as in the hadrontherapy application (Fig. 9.3) [10, 11]: it essentially requires a single type of a simple dipole magnet, an accelerating gap, some command-control instrumentation, whereas it procures greater beam manipulation flexibilities compared to (synchro-)cyclotrons.

---

[1] The story has it that it is possible to ride a bicycle in the vacuum chamber of Dubna's Synchro-Phasotron.

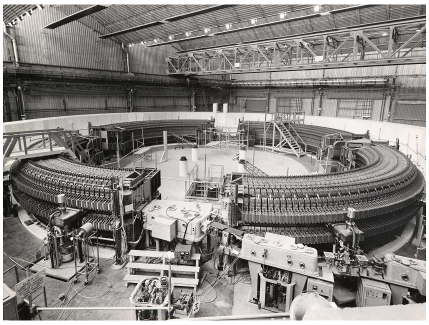

Fig. 9.1 Saturne I at Saclay [6], a 3 GeV, 4-period, 68.9 m circumference, weak focusing synchrotron, constructed in 1956-58. The injection line can be seen in the foreground, injection is from a 3.6 MeV Van de Graaff (not visible)

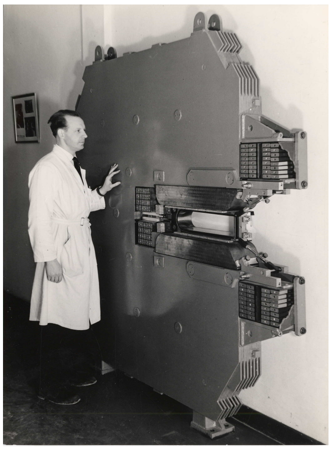

Fig. 9.2 A slice of Saturne I dipole [7]. The slight gap tapering is hardly visible (increasing outward), it determines the weak index condition $0 < n < 1$

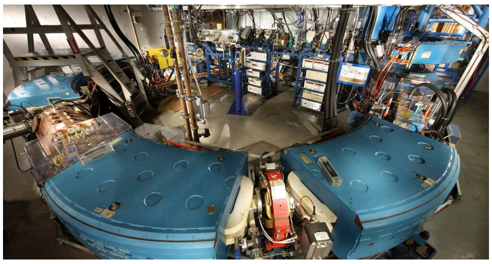

Fig. 9.3 Left: Loma Linda University medical synchrotron [8]

9.1 Basic Concepts and Formulæ

The synchrotron is based on two key principles. On the one hand, a slowly varying magnetic field to maintain a constant orbit during acceleration,

$$B(t) \times \rho = p(t)/q, \quad \rho = constant, \tag{9.1}$$

with $p(t)$ the particle momentum and ρ the bending radius in the dipoles. On the other hand, on synchronous acceleration for longitudinal phase stability. In a regime where the velocity change with energy cannot be ignored (non-ultrarelativistic particles), the latter requires a modulation of the accelerating voltage frequency so to satisfy

$$f_{RF}(t) = h f_{rev}(t) \tag{9.2}$$

Synchronism between accelerating voltage oscillation and the revolution motion keeps the bunch on the synchronous phase at traversal of the accelerating gaps.

Synchronous acceleration is technologically simpler in the case of electrons, as frequency modulation is unnecessary beyond a few MeV; for instance, from $v/c = 0.9987$ at 10 MeV to $v/c \rightarrow 1$ the relative change in revolution frequency amounts to $\delta f_{\rm rev}/f_{\rm rev} = \delta\beta/\beta < 0.0013$.

These are two major evolutions compared to the cyclotron, where, instead, the magnetic field is fixed - the reference orbit spirals out, and, by virtue of the isochronism of the orbits, the oscillating voltage frequency is fixed as well.

A fixed orbit reduces the radial extent of individual guiding magnets, allowing a ring structure comprised of a circular string of dipoles. For the sake of comparison: a synchrocyclotron instead uses a single, massive dipole; increased energy requires increased radial extent of the magnet to allow for the greater bending field integral (*i.e.*, $\oint B\,dl = 2\pi R_{max}\hat{B} = p_{max}/q$), thus a volume of iron increasing more than quadratically with bunch rigidity.

One or the other of the weak index ($-1 < k < 0$, Sect. 4.2.2) and/or wedge focusing (Sect. 18.3.1) are used in weak focusing synchrotrons. Transverse stability was based on the latter at Argonne ZGS (Zero-Gradient Synchrotron: the main magnet had no field index), a 12 GeV, 8-dipole, 4-period ring, operated over 1964-1979 (Fig. 9.4). ZGS was the first synchrotron to accelerate polarized proton beams, from July 1973 on [9], weak focusing resulted in weak depolarizing resonances, an advantage in that matter.

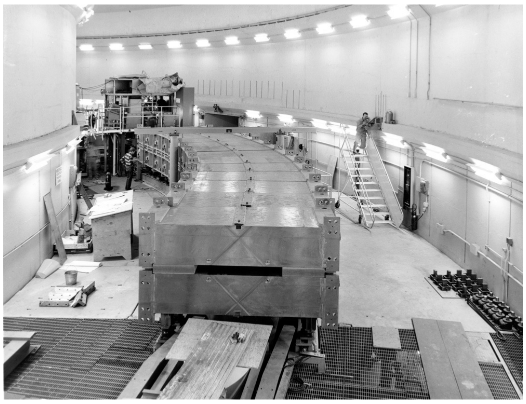

Fig. 9.4 The ZGS at Argonne during construction. A 12 GeV, 8-dipole, 4-period, 172 m circumference, wedge focusing synchrotron. The two persons inside and ouside the ring, in the background, give an idea of the size of the magnets

Due to the necessary ramping of the field in order to maintain a constant orbit, the synchrotron is a pulsed accelerator, the acceleration is cycled, from injection to top energy, repeatedly. The repetition rate of the acceleration cyclic depends on the type of power supply. If the ramping uses a constant electromotive force (E=V+Z I is constant), then

$$B(t) \propto (1 - e^{-\frac{t}{\tau}}) = 1 - \left[1 - \left(\frac{t}{\tau}\right) + \left(\frac{t}{\tau}\right)^2 - ...\right] \approx \frac{t}{\tau} \tag{9.3}$$

essentially linear. In that case $\dot{B} = dB/dt$ does not exceed a few Tesla/second, thus the repetition rate of the acceleration cycle if of the order of a Hertz. If instead the magnet winding is part of a resonant circuit (with typically 10 ∼ 60 Hz eigenfrequency) the field oscillate,

$$B(t) = B_0 + \frac{\hat{B}}{2}(1 - \cos\omega t) \tag{9.4}$$

so that, in the interval of half a voltage repetition period (*i.e.*, $t : 0 \longrightarrow \pi/\omega$) the field increases from an injection threshold value to a maximum value at highest rigidity, $B(t) : B_0 \longrightarrow B_0 + \hat{B}$. The latter determines the highest achievable energy: $\hat{E} = pc/\beta = q\hat{B}\rho c/\beta$. The repetition rate with resonant magnet cycling can reach a few tens of Hertz, a species known as "rapid-cycling" synchrotrons. In both cases anyway B imposes its law and the other quantities comprising the acceleration cycle (RF frequency in particular) will follow B(t).

For the sake of comparison: in a synchrocyclotron the field is constant, thus acceleration can be cycled as fast as the swing of the voltage frequency allows (hundreds of Hz are common practice); assume a conservative 10 kVolts per turn, thus of the order of 10,000 turns to 100 MeV, with velocity $0.046 < v/c < 0.43$ from 1 to 100 MeV, proton. Take $v \approx 0.5c$ to make it simple, an orbit circumference below 30 meter, thus the acceleration takes of the order of $10^4 \times C/0.5c \approx$ms range, potentially a repetition rate in kHz range, more than an order of magnitude beyond the reach of a rapid-cycling pulsed synchrotron.

9.1.1 Periodic Stability

This section introduces the various components of the transverse focusing and the conditions for periodic stability in a weak focusing synchrotron. It builds on material introduced in Chap. 4, Classical Cyclotron, and on Ref. [15].

9.1.1.1 Closed orbit

The concept is found in the betatron, which accelerates particles on a constant orbit (Chap. 7). The closed orbit is fixed, and maintained during acceleration by ensuring that the relationship Eq. 9.1 is satisfied. In a perfect ring, the closed orbit is along an arc in the bending magnets and straight along the drifts, Fig. 9.5.

Particle motion is defined in a moving frame (O;s,x,y) whose origin coincides with the location of an ideal particle following the refence orbit. The moving frame s axis is tangent to the reference orbit, its transverse horizontal axis x is normal to the s axis, its vertical axis y is normal to the (s, x) plane (Fig. 4.8, Sect. 4.2.2).

9.1.1.2 Transverse Focusing

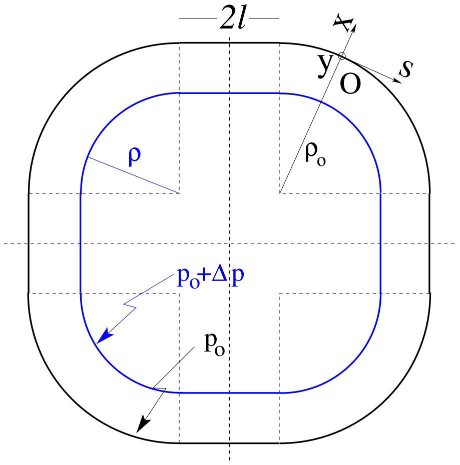

Fig. 9.5 A $2\pi/4$ axially symmetric structure with four drift spaces. Orbit length on reference momentum p_0 is $C = 2\pi\rho_0 + 8l$. (O;s,x,y) is the moving frame, along the reference orbit. The orbit for momentum $p = p_0 + \Delta p$ ($\Delta p < 0$, here) is at constant distance $\Delta x = \frac{\rho_0}{1-n}\frac{\Delta p}{p_0} = \frac{R}{(1+k)(1-n)}\frac{\Delta p}{p_0}$ from the reference orbit

Radial motion stability around a reference closed orbit in an axially symmetric dipole field requires a field index (Sect. 4.2.2),

$$n = -\frac{\rho_0}{B_0}\left.\frac{\partial B_y}{\partial \rho}\right|_{\mathrm{x=0,\ y=0}} \tag{9.5}$$

a quantity evaluated on the reference arc in the dipoles, satisfying the weak focusing condition

$$0 < n < 1 \tag{9.6}$$

This condition can be obtained with a tapered gap (Fig. 9.2) causing the magnetic field to decrease slowly with radius. Note the sign convention here, the cyclotron uses the oppposite sign (Eq. 4.10). This condition holds regardless of the presence of drifts or not. Adding drift spaces between the dipoles, the reference orbit is comprised of arcs of radius ρ_0 in the magnets, and straight segments along the drift spaces that connect these arcs. This requires defining two radii, namely,

(i) the magnet curvature radius ρ_0,

(ii) an average radius $R = C/2\pi = \rho_0 + Nl/\pi$ (with C the length of the reference closed orbit and $2l$ the drift length) (Fig. 9.5) which also writes

$$R = \rho_0(1+k), \qquad k = \frac{Nl}{\pi\rho_0} \tag{9.7}$$

Adding drift spaces decreases the average focusing around the ring.

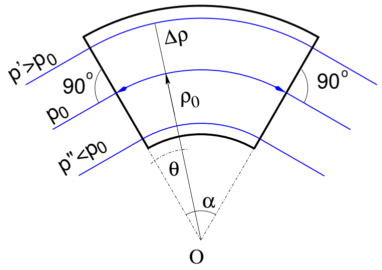

Fig. 9.6 In a sector dipole with radial index $n \neq 0$, closed orbits follow arcs of constant field. A closed orbit at $p_0 + \Delta p$ follows an arc of radius $\rho_0 + \Delta\rho$, $\Delta\rho = \Delta p/(1+n)qB_0$

Geometrical focusing

The limit $n \longrightarrow 1$ of the transverse motion stability domain corresponds to a cancellation of the geometrical focusing (Fig. 9.7): in a constant field dipole (radial field index n=0) the longer (respectively shorter) path in the magnetic field for parallel trajectories entering the magnet at greater (respectively smaller) radius result in convergence. This effect is cancelled, *i.e.*, the deviation is the same whatever the entrance radius, if the curvature center is made independent of the entrance radius: $OO' = 0$, $O''O = 0$. This occurs if trajectories at an outer (inner) radius experience a smaller (greater) field such as to satisfy $BL = B\rho\,\alpha = C^{st}$. Differentiating $B\rho = C^{st}$ gives $\frac{\Delta B}{B} + \frac{\Delta\rho}{\rho} = 0$, with $\Delta\rho = \Delta x$, so yielding $n = -\frac{\rho_0}{B_0}\frac{\Delta B}{\Delta x} = 1$. The focal distance associated with the curvature is (Eq. 4.12 with $R = \rho_0$) $f = \frac{\rho_0^2}{\mathcal{L}}$. Optical drawbacks of the weak focusing method include the weakness of the focusing and the absence of independent radial and axial focusing.

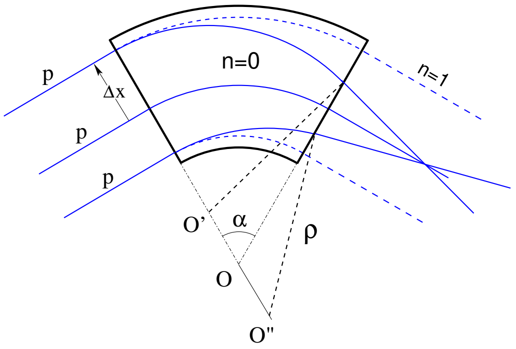

Fig. 9.7 Geometrical focusing: in a sector dipole with focusing index $n = 0$, parallel incoming rays of equal momenta experience the same curvature radius ρ, they exit converging, as a results of the longer path of outer trajectories in the field, compared to inner ones. An index value n=1 cancels that effect: rays exit parallel

Wedge Focusing

Entrance and exit wedge angles may be used to ensure transverse focusing: opening the magnetic sector increases the horizontal focusing (and decreases the vertical focusing); closing the magnetic sector has the reverse effect (Sect. 18.3.1). In a point transform approximation, at the wedge the trajectory undergoes a local deviation proportional to the distance to the optical axis, namely,

$$\Delta x' = \frac{\tan\varepsilon}{\rho_0}\Delta x, \quad \Delta y' = -\frac{\tan(\varepsilon - \psi)}{\rho_0}\Delta y \tag{9.8}$$

ψ is a correction for the fringe field extent (Eq. 18.20), an effect on the vertical focusing of the first order in the coordinates (it is a second order effect horizontally).

Profiling the magnet gap in order to adjust the focal distance complicates the magnet; a parallel gap, $n = 0$, makes it simpler, for that reason edge focusing may be preferred. Wedge vertical focusing in the ZGS ($\varepsilon > 0$) was at the expense of horizontal geometrical focusing (Fig. 9.6). This was an advantage though, for the acceleration of polarized beams, as radial field components (which are responsible for depolarization) were only met at the EFBs of the eight main dipoles [9]. Preserving beam polarization at high energy required tight control of the tunes, and this was achieved by, in addition, pole face windings at the ends of the dipoles [12, 13]; these coils where pulsed to control the amplitude detuning, resulting in a control of the tunes at 0.01 level; they also compensated eddy current induced sextupole perturbations which affected the vertical tune.

9.1.1.3 Periodic stability, betatron motion

The first order differential equations of motion in the moving frame (Fig. 9.5) derive from the Lorentz equation [15]

$$\frac{dm\mathbf{v}}{dt} = q\mathbf{v}\times\mathbf{B} \;\Rightarrow\; m\frac{d}{dt}\left\{\begin{matrix} \frac{ds}{dt}\mathbf{s} \\ \frac{dx}{dt}\mathbf{x} \\ \frac{dy}{dt}\mathbf{y} \end{matrix}\right\} = q\left\{\begin{matrix} (\frac{dx}{dt}B_y - \frac{dy}{dt}B_x)\mathbf{s} \\ -\frac{ds}{dt}B_y\mathbf{x} \\ \frac{ds}{dt}B_x\mathbf{y} \end{matrix}\right\} \tag{9.9}$$

Introduce the field index $n = -\frac{\rho_0}{B_0}\frac{\partial B_y}{\partial x}$ evaluated on the reference orbit, with $B_0 = B_y(\rho_0, y = 0)$; assume transverse stability: $0 < n < 1$. Taylor expansion of the transverse field components in the moving frame write

$$\begin{aligned} B_y(\rho) &= B_y(\rho_0) + x\frac{\partial B_y}{\partial x}\bigg|_{\rho_0} + O(x^2) \approx B_y(\rho_0) - n\frac{B_y}{\rho_0}\bigg|_{\rho_0} x = B_0(1 - n\frac{x}{\rho_0}) \\ B_x(0+y) &= \underbrace{B_x(0)}_{=0} + y \underbrace{\frac{\partial B_x}{\partial y}\bigg|_{\rho_0}}_{=\frac{\partial B_y}{\partial x}} \text{(+ higher order in y)} \approx -n\frac{B_0}{\rho_0}y \end{aligned} \tag{9.10}$$

Introduce in addition $ds \approx v dt$, Eqs. 9.9, 9.10 lead to the differential equations of motion in a dipole field

$$\frac{d^2x}{ds^2}+\frac{1-n}{\rho_0^2}x=0,\quad \frac{d^2y}{ds^2}+\frac{n}{\rho_0^2}y=0 \tag{9.11}$$

It results that, in an S-periodic structure comprised of gradient dipoles, wedges and drift spaces, the differential equation of motion takes the general form of Hill's equation, a second order differential equation with periodic coefficient, namely (with u standing for x or y),

$$\begin{cases}\dfrac{d^2u}{ds^2}+K_u(s)u=0\\ K_u(s+S)=K_u(s)\end{cases}\quad \text{with}\quad \begin{cases}\text{in dipoles : }\begin{cases}K_x=(1-n)/\rho_0^2\\ K_y=n/\rho_0^2\end{cases}\\ \text{at a wedge : }\ \mathrm{K}_{\substack{x\\y}}=\pm(\tan\varepsilon)/\rho_0\\ \text{in drift spaces : }\mathrm{K_x}=\mathrm{K_y}=0\end{cases} \tag{9.12}$$

$K_u(s)$ is S-periodic, $S=2\pi R/N$ ($S=C/4$ for instance in a 4-periodic ring, Figs. 9.1, 9.5). G. Floquet has established [14] that the two independent solutions of Hill's second order differential equation have the form [15]

$$\left|\begin{array}{l}u_1(s)=\sqrt{\beta_u(s)}\,e^{\,i\int_0^s\frac{ds}{\beta_u(s)}}\\ du_1(s)/ds=\dfrac{i-\alpha_u(s)}{\beta_u(s)}\,u_1(s)\end{array}\right.\quad\text{and}\quad\left|\begin{array}{l}u_2(s)=u_1^*(s)\\ du_2(s)/ds=du_1^*(s)/ds\end{array}\right. \tag{9.13}$$

wherein $\beta_u(s)$ and $\alpha_u(s)=-\beta_u'(s)/2$ are S-periodic functions, from what it results that

$$u_{\substack{1\\2}}(s+S)=u_{\substack{1\\2}}(s)\,e^{\pm i\mu_u} \tag{9.14}$$

wherein

$$\mu_u=\int_{s_0}^{s_0+S}\frac{ds}{\beta_u(s)} \tag{9.15}$$

is the betatron phase advance over a period. A real solution of Hill's equation is the linear combination $A\,u_1(s)\ +\ A^*\,u_2^*(s)$. With $A=\frac{1}{2}\sqrt{\varepsilon_u/\pi}e^{i\phi}$ following conventional notations, the general solution of Eq. 9.12 then writes

$$\left|\begin{array}{l}u(s)=\sqrt{\beta_u(s)\varepsilon_u/\pi}\,\cos\left(\int\dfrac{ds}{\beta_u}+\phi\right)\\ u'(s)=-\sqrt{\dfrac{\varepsilon_u/\pi}{\beta_u(s)}}\,\sin\left(\int\dfrac{ds}{\beta_u}+\phi\right)+\alpha_u(s)\,\cos\left(\int\dfrac{ds}{\beta_u}+\phi\right)\end{array}\right. \tag{9.16}$$

An invariant of the motion is

$$\frac{1}{\beta_u(s)}\left[u^2+(\alpha_u(s)u+\beta_u(s)u')^2\right]=\frac{\varepsilon_u}{\pi} \tag{9.17}$$

known as the Courant-Snyder invariant. At a given azimuth s of the periodic structure the observed turn-by-turn motion lies on that ellipse (Fig. 9.8). The form and inclination of the ellipse depend on the observation azimuth s via the respective local values of $\alpha_u(s)$ and $\beta_u(s)$, but its surface ε_u is invariant. Motion along the ellipse is clockwise, as can be figured from Eq. 9.16 considering an observation azimuth s where the ellipse is upright, $\alpha_u(s) = 0$. In an N-periodic ring, the phase advance over a turn (from one location to the next on the ellipse in Fig. 9.8) is

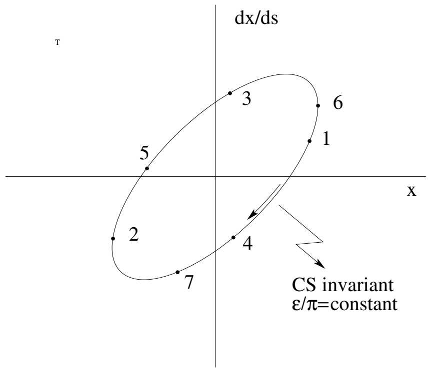

Fig. 9.8 Courant-Snyder invariant and turn-by-turn harmonic motion along the invariant, observed at some azimuth s. The form of the ellipse depends on the observation azimuth s but its surface ε_u is invariant

$$\int_{s_0}^{s_0+NS} \frac{ds}{\beta_u(s)} = N \int_{\text{period}} \frac{ds}{\beta_u(s)} = N\mu_u \tag{9.18}$$

Weak focusing approximation

In the case of a cylindrically symmetric structure, a sinusoidal motion is the exact solution of the first order differential equations of motion (Eqs. 4.14, 4.15, Classical Cyclotron Chapter). In that case the latter have a constant (s-independent) coefficient, $K_x = (1-n)/R_0^2$ and $K_y = n/R_0^2$, respectively. Adding drift spaces results in Hill's differential equation with periodic coefficient $K(s+S) = K(s)$ (Eq. 9.12), and in a pseudo harmonic solution (Eq. 9.16). Due to the weak focusing the beam envelope is only weakly modulated (see below), thus so is $\beta_u(s)$. In a practical manner, the modulation of $\beta_u(s)$ does not exceed a few percent, this justifies introducing the average value $\overline{\beta_u}$ to approximate the phase advance by

$$\int_0^s \frac{ds}{\beta_u(s)} \approx \frac{s}{\overline{\beta_u}} = \nu_u \frac{s}{R} \tag{9.19}$$

The right equality is obtained by applying this approximation to the the phase advance per period (Eq. 9.15), namely $\mu_u = \int_{s_0}^{s_0+S} \frac{ds}{\beta_u(s)} \approx S/\overline{\beta_u}$, and introducing the wave number of the N-period optical structure

$$\nu_u = \frac{N\mu_u}{2\pi} = \frac{\text{phase advance over a turn}}{2\pi} \tag{9.20}$$

so that

$$\overline{\beta_u} = \frac{R}{\nu_u} \tag{9.21}$$

Substituting in Eq. 9.16 yields the approximate solution

$$\left| \begin{array}{l} u(s) \approx \sqrt{\beta_u(s)\varepsilon_u/\pi}\, \cos\left(\nu_u \frac{s}{R} + \phi\right) \\ u'(s) = -\sqrt{\frac{\varepsilon_u/\pi}{\beta_u(s)}}\, \sin\left(\nu_u \frac{s}{R} + \phi\right) + \alpha_u(s)\, \cos\left(\nu_u \frac{s}{R} + \phi\right) \end{array} \right. \tag{9.22}$$

In this approximation, the differential equations of motion (Eq. 9.12) can be expressed under the form

$$\frac{d^2x}{ds^2} + \frac{\nu_x^2}{R^2}x = 0, \qquad \frac{d^2y}{ds^2} + \frac{\nu_y^2}{R^2}y = 0 \tag{9.23}$$

Beam envelopes

The beam envelope $\hat{u}(s)$ (with u standing for x or y) is determined by the particle of maximum invariant ε_u/π, it is given by

$$\pm\hat{u}(s) = \pm\sqrt{\beta_u(s)\varepsilon_u/\pi} \tag{9.24}$$

As $\beta_u(s)$ is S-periodic, so is the envelope, $\hat{u}(s+S) = \hat{u}(s)$. In a cell with symmetries, beam envelops feature the same symmetries, as in Fig. 9.9 for instance: a symmetry with respect to the center of the cell; envelop extrema are at azimuth s of $\beta_u(s)$ extrema, where $\alpha_u = 0$ as $\beta_u' = -2\alpha_u$.

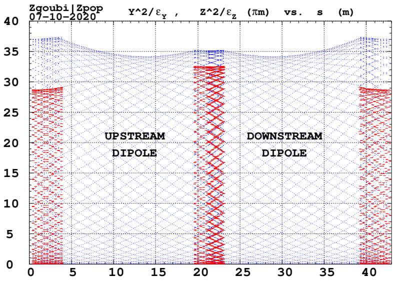

Fig. 9.9 Excursion of a particle along a 43 m long cell, over many turns. The extrema of this motion tangent the envelops, respectively $\pm\left(\beta_x(s)\,\varepsilon_x/\pi\right)^{1/2}$, horizontal (red), and $\pm\left(\beta_y(s)\,\varepsilon_y/\pi\right)^{1/2}$, vertical (blue), at all s. Envelops are symmetric with respect to $s = 21.5$ m, a consequence of that very symmetry of the cell

Working point

The “working point” of the synchrotron is the wave number couple (ν_x, ν_y) at which the accelerator is operated, it fully characterizes the focusing. In a structure with cylindrical symmetry $\nu_x = \sqrt{1-n}$ and $\nu_y = \sqrt{n}$ (Eq. 4.16) so that $\nu_x^2 + \nu_y^2 = 1$: when the radial field index n is changed the working point stays on a circle of radius 1 in the stability diagram (or “tune diagram”, Fig. 9.10). If drift spaces are added, from the linear approximation (Eqs. 9.11, 9.12) it comes

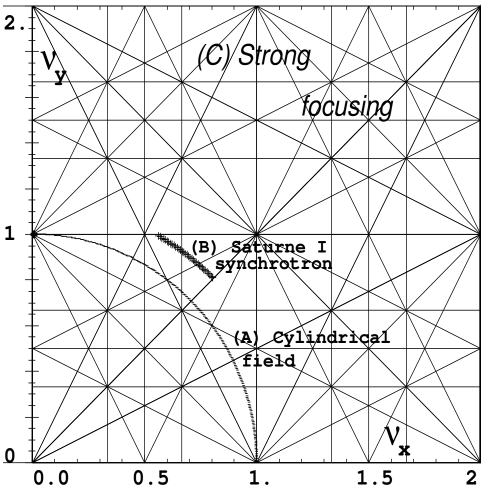

Fig. 9.10 Location of the working point in the tune diagram, in case of (A) field with revolution symmetry, on a circle of radius 1; (B) sector field with index + drift spaces, on a circle of radius ($\sqrt{R/\rho_0}$). Case (C) is for strong focusing, ($|n| \gg 1$), ν_x and ν_y are large

$$\nu_x = \sqrt{(1-n)\frac{R}{\rho_0}}, \quad \nu_y = \sqrt{n\frac{R}{\rho_0}}, \qquad \nu_x^2 + \nu_y^2 = \frac{R}{\rho_0} \tag{9.25}$$

thus the working point is located on the circle of radius $\sqrt{R/\rho_0} > 1$. Tunes can not exceed the limits

$$0 < \nu_{\mathrm{x,y}} < \sqrt{R/\rho_0}$$

Horizontal and vertical focusing are not independent (Eq. 9.12): if ν_x increases then ν_y decreases and reciprocally. This is a lack of flexibility which the advent of strong focusing will overcome by providing two knobs allowing separate adjustment of the tunes.

Off-momentum orbits

In a dipole with field index $n = -\frac{\rho_0}{B_0}\frac{\partial B_y}{\partial \rho}$, orbits different momenta $p = p_0 + \Delta p$ are concentric (Fig. 9.6), distant (after Eq. 4.18)

$$\Delta x = \frac{\rho_0}{1-n}\frac{\Delta p}{p_0}$$

from the reference orbit. Introduce now the geometrical radius $R = (1+k)\rho_0$ (Eq. 9.7) to account for the added drifts, this gives

$$\frac{\Delta x}{\Delta p/p_0} \equiv \frac{\Delta R}{\Delta p/p_0} = \frac{R}{(1-n)(1+k)} \tag{9.26}$$

Thus the chromatic dispersion of the orbits, the dispersion function

$$D = \frac{\Delta x}{\Delta p/p_0} = \frac{R}{(1-n)(1+k)}, \quad \text{constant} \tag{9.27}$$

an s-independent quantity: in a structure with axial symmetry, comprising drift sections (Fig. 9.5) or not (classical and AVF cyclotrons for instance), the ratio $\frac{\Delta x}{\rho_0 \Delta p/p_0}$ is independent of the azimuth s, the distance of a chromatic orbit to the reference orbit is constant around the ring.

Given that $n < 1$,
- higher momentum orbits, $p > p_0$, have a greater radius,
- lower momentum orbits, $p < p_0$, have a smaller radius.

Chromatic orbit length

In an axially symmetric structure the difference in closed orbit length $\Delta C = 2\pi\Delta R$ resulting from the difference in momentum arises in the dipoles, as all orbits are parallel in the drifts (Fig. 9.5). Hence, from Eq. 9.26, the relative closed orbit lengthening factor, “momentum compaction”

$$\alpha = \frac{\Delta C}{C}\Big/\frac{\Delta p}{p_0} \equiv \frac{\Delta R}{R}\Big/\frac{\Delta p}{p_0} = \frac{1}{(1-n)(1+k)} \approx \frac{1}{\nu_x^2} \tag{9.28}$$

with $k = Nl/\pi\rho_0$ (Eq. 9.7). Note that the relationship $\alpha \approx 1/\nu_x^2$ between momentum compaction and horizontal wave number established for a revolution symmetry structure (Eq. 4.20) still holds when adding drifts.

9.1.1.4 Longitudinal Motion

In a synchrotron, the field B is varied during acceleration (a function performed by the power supply) concurently with the variation of the bunch momentum p (a function performed by the accelerating cavity) in such a way that at any time

$$\Delta W = F \times 2\pi R = 2\pi q R \rho \dot{B} B(t) \rho = p(t)/q \tag{9.29}$$

so that the beam is maintained on the design orbit. Given the energies involved, the magnet supply imposes its law and the cavity follows $B(t)$ (Fig. 9.11), the best it can. The accelerating voltage $\hat{V}(t) = \sin \omega_{\mathrm{rf}} t$ is maintained in synchronism with the revolution motion, its angular frequency satisfying

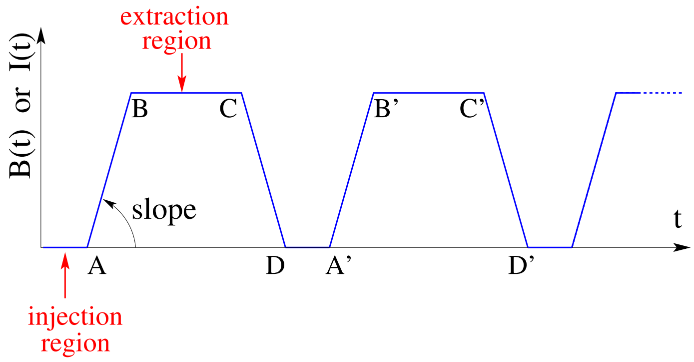

Fig. 9.11 Cycling $B(t)$ in a pulsed synchrotron. Ignoring saturation, $B(t)$ is proportional to the magnet power supply current $I(t)$. Beam injection occurs at low field, in the region of A, extraction occurs at top energy, on the high field plateau. (AB): field ramp up (acceleration); (BC): flat top; (CD): field ramp down; (DA'): thermal relaxation. (AA'): repetition period; (1/AA'): repetition rate; *slope*: ramp velocity $\dot{B} = dB/dt$ (Tesla/s).

$$\omega_{\mathrm{rf}} = h\omega_{\mathrm{rev}} = h\frac{c}{R}\frac{B(t)}{\sqrt{\left(\frac{m_0}{q\rho}\right)^2 + B^2(t)}}$$

Energy gain

The variation of the particle energy over a turn amounts to the work of the force $F = dp/dt$ on the charge at the cavity, namely

$$\Delta W = F \times 2\pi R = 2\pi q R \rho \dot{B} \tag{9.30}$$

Over most of the acceleration cycle in a slow-cycling synchrotron $\dot{B}$ is usually constant (Eq. 9.3), thus so is ΔW. At Saturne I for instance (the object of Exercise 9.1, parameters in Tab. 9.1)

$$\frac{\Delta W}{q} = 2\pi R \rho \dot{B} = 68.9 \times 8.42 \times 1.8 = 1044 \text{ volts}$$

The field ramp lasts

$$\Delta t = (B_{\max} - B_{\min})/\dot{B} \approx B_{\max}/\dot{B} = 0.8\,\mathrm{s}$$

The number of turns to the top energy ($W_{\max} \approx 3\,\mathrm{GeV}$) is

$$N = \frac{W_{\max}}{\Delta W} = \frac{3\,10^9\ \mathrm{eV}}{1044\ \mathrm{eV/turn}} \approx 3\,10^6 \mathrm{turns}$$

The dependence of particle mass on field writes

$$m(t) = \gamma(t) m_0 = \frac{q\rho}{c}\sqrt{\left(\frac{m_0}{qc\rho}\right)^2 + B(t)^2}$$

2686 *Adiabatic damping of the betatron oscillations*

The focusing index (Eq. 9.5) does not change during acceleration, thus the tunes ν_x and ν_y do not change either. As a result of the longitudinal acceleration at the cavity though, the longitudinal energy of the particles is modified. This results in a decrease of the amplitude of betatron oscillations (an increase if the cavity is decelerating). The mechanism is sketched in Fig. 9.12: the slope, respectively before and after (index 2) the cavity is

$$\frac{dx}{ds} = \frac{m\frac{dx}{dt}}{m\frac{ds}{dt}} = \frac{p_x}{p_s}, \qquad \left.\frac{dx}{ds}\right|_2 = \left.\frac{m\frac{dx}{dt}}{m\frac{ds}{dt}}\right|_2 = \frac{p_{x,2}}{p_{s,2}}$$

Particle mass and velocity are modified at the traversal of the cavity but, as the

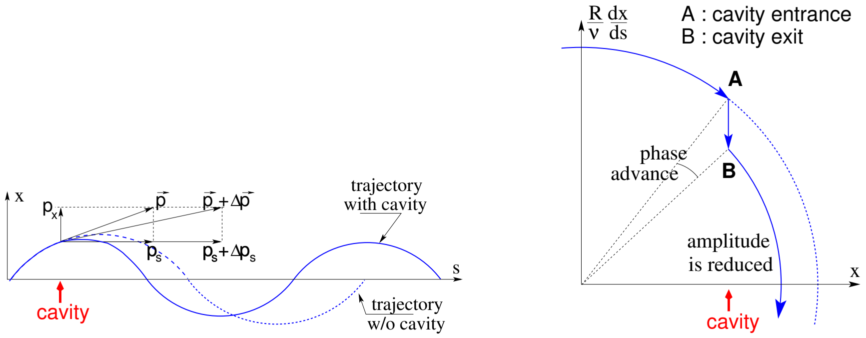

Fig. 9.12 Adiabatic damping of betatron oscillations, here from $x' = p_x/p_s$ before the cavity, to $x'_2 = p_x/(p_s + \Delta p_s)$ after the cavity. In the horizontal phase space, to the right, decrease of $\Delta\left(\frac{dx}{ds}\right)$ if $\frac{dx}{ds} > 0$, increase of $\Delta\left(\frac{dx}{ds}\right)$ if $\frac{dx}{ds} < 0$

force is longitudinal, $dp_x/dt = 0$ thus $p_x' = p_x$, the increase in momentum is purely longitudinal, $p_s' = p_s + \Delta p$. Thus

$$\left.\frac{dx}{ds}\right|_2 = \frac{p_x}{p_s + \Delta p} \approx \frac{p_x}{p_s}(1 - \frac{\Delta p}{p_s})$$

and as a consequence the slope dx/ds varies across the cavity,

$$\Delta\left(\frac{dx}{ds}\right) = \left.\frac{dx}{ds}\right|_2 - \frac{dx}{ds} = -\frac{dx}{ds}\frac{\Delta p_s}{p_s}$$

The variation of the slope is proportional to the slope, with opposite sign if $\Delta p/p > 0$ (acceleration) thus a decrease of the slope. This variation has two consequences on the betatron oscillation (Fig. 9.12):
- a change of the betatron phase,
- a modification of the betatron amplitude.

Coordinate transport

at the cavity writes $\begin{cases} x_2 = x \\ x_2' \approx \frac{p_x}{p_s}(1 - \frac{dp}{p}) = x'(1 - \frac{dp}{p}) \end{cases}$. In matrix form, $\begin{pmatrix} x_2 \\ x_2' \end{pmatrix} = [C]\begin{pmatrix} x \\ x' \end{pmatrix}$ with

$$[C] = \begin{bmatrix} 1 & 0 \\ 0 & 1 - \frac{dp}{p} \end{bmatrix} \tag{9.31}$$

and $det[C] = 1 - \frac{dp}{p} \neq 1$: the system is non-conservative, the surface of the beam ellipse in phase space is not conserved. Assume one cavity in the ring and note $[T] \times [C]$ the one-turn coordinate transport matrix with origin at entrance of the cavity. Its determinant is $det[T] \times det[C] = det[C] = 1 - \frac{dp}{p}$; the variation of the transverse ellipse surface satisfies $\varepsilon_u = (1 - \frac{dp}{p_0})\varepsilon_0$ or, with $d\varepsilon_u = \varepsilon_u - \varepsilon_0$, $\frac{d\varepsilon_u}{\varepsilon_u} = -\frac{dp}{p_0}$, the solution of which is

$$p\ \varepsilon_u = constant, \quad or \quad \beta\gamma\varepsilon_u = constant \tag{9.32}$$

Over N turns the coordinate transport matrix is $[T_N] = ([T][C])^N$, its determinant is $(1 - \frac{dp}{p})^N \approx 1 - N\frac{dp}{p}$: the ellipse surface changes by that factor.

Synchrotron motion; *phase stability*

"Synchrotron motion" designates the mechanism of phase stability, or longitudinal focusing (Fig. 9.13), that stabilizes the longitudinal motion of a particle in the vicinity of a synchronous phase, ϕ_s, in virtue of

(i) the presence of an accelerating cavity with its frequency indexed on the revolution time,

(ii) with the bunch centroid positioned either on the rising slope of the oscillating voltage (low energy regime), or on the falling slope (high energy regime).

The synchronous (or “ideal”) particle follows the equilibrium trajectory around the ring (the reference closed orbit, about which all other particles will undergo a betatron oscillation), its velocity satisfies $v(t) = \frac{qB\rho(t)}{m}$; at each turn it reaches the accelerating gap when the oscillating voltage is at the synchronous phase ϕ_s, and undergoes an energy gain

$$\Delta W = q\hat{V}\sin\phi_s$$

The condition $|\sin\phi_s| < 1$ imposes a lower limit to the cavity voltage for acceleration to happen, namely, after Eq. 9.30,

$$\hat{V} > 2\pi R\rho\dot{B}$$

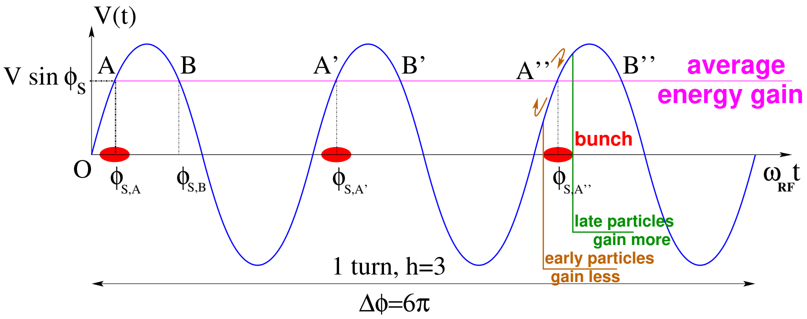

Fig. 9.13 Mechanism of phase stability, “longitudinal focusing”. Below transition ($\gamma < \gamma_{tr}$) phase stability occurs for a synchronous phase taken at either of the h=3 stable locations A, A’, A”: a particle with higher energy goes around the ring more rapidly than the synchronous particle, it arrives earlier at the voltage gap (at $\phi < \phi_{s,A}$) and experiences a lower voltage; at lower energy the particle is slower, it arrives at the gap later compared to the synchronous particle, at $\phi > \phi_{s,A}$, and experiences a greater voltage; this results overall in a stable oscillatory motion around the synchronous phase. Beyond transition ($\gamma > \gamma_{tr}$) the stable phase is at either of the h=3 stable locations B, B’, B’:, a particle which is less energetic than the synchronous particle arrives earlier, $\phi < \phi_{s,B}$, it experiences a greater voltage, and inversely when it eventually gets more energetic than the synchronous particle

Referring to Fig. 9.13, the synchronous phase can be placed on the left (A A’ A”... series in the Figure, or on the right (B B’ B”... series) of the oscillating voltage crest. One and only one of these two possibilities, and which one depends on the optical lattice and on particle energy, ensures that particles in a bunch remain grouped in the vicinity of the synchronous particle. The transition between these two regimes (A series or B series) occurs at the transition γ, γ_{tr}, a property of the lattice. If the bunch energy is below transition energy, $E_{\mathrm{bunch}} < m\gamma_{\mathrm{tr}}$, the bunch has to present itself on the left of the crest (A series), if the bunch energy is greater than transition energy, $E_{\mathrm{bunch}} > m\gamma_{\mathrm{tr}}$, the bunch has to present itself on the right of the crest (B series).

Transition energy

The transition between the two regimes occurs at $\dfrac{dT_{\mathrm{rev}}}{T_{\mathrm{rev}}} = 0$. With $T = 2\pi/\omega = C/v$, this can be written $\dfrac{d\omega_{\mathrm{rev}}}{\omega_{\mathrm{rev}}} = -\dfrac{dT_{\mathrm{rev}}}{T_{\mathrm{rev}}} = \dfrac{dv}{v} - \dfrac{dC}{C}$. With $\frac{dv}{v} = \frac{1}{\gamma^2}\frac{dp}{p}$ and momentum compaction $\alpha = \dfrac{dC}{C} \,/\, \frac{dp}{p}$, (Eq. 9.28), this can be written

$$\frac{d\omega_{\mathrm{rev}}}{\omega_{\mathrm{rev}}} = -\frac{dT_{\mathrm{rev}}}{T_{\mathrm{rev}}} = \left(\frac{1}{\gamma^2} - \alpha\right)\frac{dp}{p} = \eta\frac{dp}{p} \tag{9.33}$$

wherein the phase-slip factor has been introduced,

$$\eta = \overbrace{\frac{1}{\gamma^2}}^{\text{kinematics}} - \underbrace{\alpha}_{\text{lattice}} = \frac{1}{\gamma^2} - \frac{1}{\gamma_{\mathrm{tr}}^2} \tag{9.34}$$

In a weak focusing structure $\gamma_{\mathrm{tr}} = 1/\sqrt{\alpha} \approx \nu_x$ (Eqs. 4.20, 9.28), thus the phase stability regime is

$$\text{below transition, } \textit{i.e. } \phi_s < \pi/2, \quad \text{if} \quad \gamma < \nu_x \tag{9.35}$$

$$\text{above transition, } \textit{i.e.} \phi_s > \pi/2, \quad \text{if} \quad \gamma > \nu_x \tag{9.36}$$

$$\tag{9.37}$$

In a weak focusing synchrotron the horizontal tune $\nu_x = \sqrt{(1-n)R/\rho_0}$ (Eq. 9.25) may be $\gtrless 1$, and subsequently $\gamma_{\mathrm{tr}} > 1$ is possible. There is no transition-gamma if $\nu_x < 1$. Acceleration to 3 GeV in Saturne I for instance, from 50 MeV at injection, and with $\nu_x \approx 0.7$ (Tab. 9.1) did not require transition-gamma crossing[2].

9.1.2 Spin Motion, Depolarizing Resonances

The availability of polarized proton sources allowed the acceleration of polarized beams to high energy. The possibility was considered from the early times of the ZGS [17], up to 70% polarization transmission through the synchrotron was fore-

---

[2] Ttransition-gamma crossing, or "gamma jump", is a common beam manipulation during acceleration in strong focusing synchrotrons, it requires an RF phase jump, the technique is addressed in Chapter 10

seen, polarization manipulation concepts included harmonic orbit correction, tune jump at strongest depolarizing resonances (Fig. 9.14). Acceleration of a polarized proton beam happened for the first time in a synchrotron and to multi-GeV energy in 1973, four years after the ZGS startup. Beams were accelerated up to 17 GeV with substantial polarization maintained [9]. Experiments were performed to assess the possibility of polarization transmission in strong focusing synchrotrons, and polarization lifetime in colliders [18]. Acceleration of polarized deuteron was achieved in the late 1970s, when sources where made available [19].

The field index is essentially zero in the ZGS, transverse focusing is ensured by wedge angles at the ends of the height dipoles, which is thus the only location where non-zero horizontal field components are found. The vertical wave number is small in addition, less than 1. This results in depolarizing resonance strengths on the weak side, *“As we can see from the table, the transition probability* [*from spin state* $\psi_{1/2}$ *to spin state* $\psi_{-1/2}$] *is reasonably small up to* $\gamma = 7.1$*”* [9], *i.e.* $G\gamma = 12.73$, $p = 6.6$ GeV/c; the table referred to stipulates a transition probability $P_{\frac{1}{2},-\frac{1}{2}} < 0.042$, whereas resonances beyond that energy range feature $P_{\frac{1}{2},-\frac{1}{2}} > 0.36$. Beam depolarization up to 6 GeV/c, under the effect of these resonances, is illustrated in Fig. 9.14.

In weak focusing synchrotron particles experience radial fields all along the bend dipoles as an effect of the radial field index, as they undergo vertical betatron oscillations. However these radial field components are weak, and so is there effect on spin motion, as long as the particle energy (the γ factor in the spin precession equation) is not too high.

Assuming a defect-free ring, the vertical betatron motion excites “intrinsic” spin resonances, located at

$$G\gamma_R = k\,P \pm \nu_y$$

with k an integer and P the period of the ring. In the ZGS for instance, $\nu_y \approx 0.8$ (Tab. 9.2), the ring P=4-periodic, thus $G\gamma_R = 4k \pm 0.8$. Strongest resonances are located at

$$G\gamma_R = MP\,k \pm \nu_y$$

with M the number of cells per superperiod [20, Sec. 3.II]. In the ZGS, M=2 thus strongest resonances occur at $G\gamma_R = 2 \times 4k \pm 0.8$.

In the presence of vertical orbit defects, non-zero periodic transverse fields are experienced along the closed orbit, they excite “imperfection” depolarizing resonances, located at

$$G\gamma_R = k$$

with k an integer. In the case of systematic defects the periodicity of the orbit is that of the lattice, P, imperfection resonances are located at $G\gamma_R = kP$. Strongest imperfection resonances are located at

$$G\gamma_R = MP\,k$$

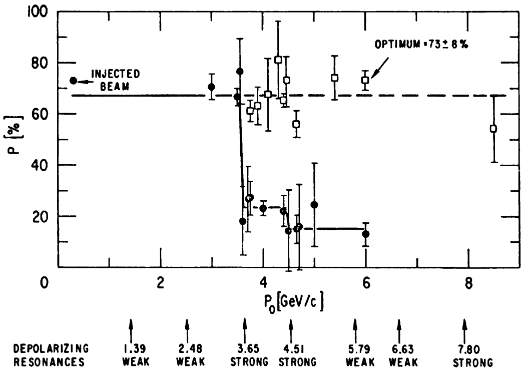

Fig. 9.14 Depolarizing intrinsic resonance landscape up to 6 GeV/c at the ZGS (solid circles). Systematic resonances are located at $G\gamma_R = 4 \times \text{integer} \pm \nu_y$, stronger ones at $G\gamma_R = 8 \times \text{integer} \pm \nu_y$. Tune jump was used to preserve polarization when crossing strong resonances (empty circles) [?]

with M the number of cells per superperiod [20, Sec. 3.II]. Crossing a depolarizing resonance, during acceleration, causes a loss of polarization given by (Froissart-Stora formula [21])

$$\frac{P_f}{P_i} = 2e^{-\frac{\pi}{2}\frac{|\epsilon_R|^2}{\alpha}} - 1 \tag{9.38}$$

from a value P_i upstream to an asymptotic value P_f downstream of the resonance. This assumes an isolated resonance, passed with a crossing speed

$$\alpha = G\frac{d\gamma}{d\theta} = \frac{1}{2\pi}\frac{\Delta E}{M} \tag{9.39}$$

with ΔE the energy gain per turn and M the mass. ϵ_R is the resonance strength.

Spin precession axis. Resonance width

Consider the spin vector $\mathbf{S}(\theta) = (S_\eta, S_\xi, S_y)$ of a particle in the laboratory frame, with θ the orbital angle around the accelerator. Introduce the projection $s(\theta)$ of $\mathbf{S}$ in the median plane

$$s(\theta) = S_\eta(\theta) + jS_\xi(\theta) \qquad (\text{and } S_y^2 = 1 - s^2) \tag{9.40}$$

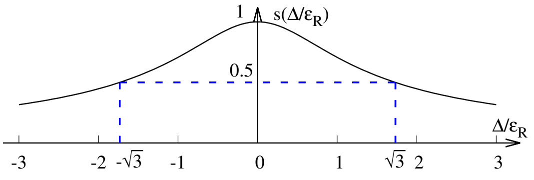

Fig. 9.15 Modulus of the horizontal spin component. $s = 1/2$ at distance $\Delta = \pm\sqrt{3}\epsilon_R$ from $G\gamma_R$

It can be shown that in the case of a stationary solution of the spin motion (*i.e.*, the spin precession axis) s satisfies [22] (Fig. 9.15)

$$s^2 = \frac{1}{1 + \frac{\Delta^2}{|\epsilon_R|^2}} \tag{9.41}$$

wherein $\Delta = G\gamma - G\gamma_R$ is the distance to the resonance. The resonance width is a measure of its strength (Fig. 9.16). The quantity of interest is the angle, ϕ, of the spin precession direction to the vertical axis, given by (Fig. 9.16)

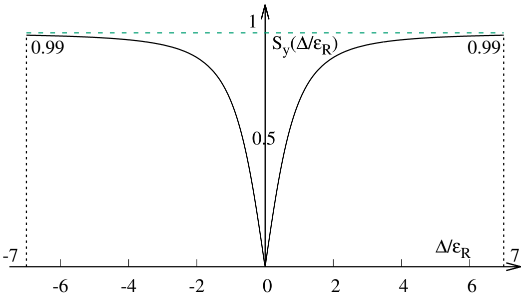

Fig. 9.16 Dependence of polarization on the distance to the resonance. For instance $S_y = 0.99$, 1% depolarization, corresponds to $\Delta = 7|\epsilon_R|$. On the resonance, $\Delta = 0$, the precession axis lies in the median plane, $S_y = 0$

$$\cos\phi(\Delta) \;\equiv S_y(\Delta) = \sqrt{1 - s^2} = \frac{\Delta/|\epsilon_R|}{\sqrt{1 + \Delta^2/|\epsilon_R|^2}} \tag{9.42}$$

On the resonance, $\Delta = 0$, the spin precession axis lies in the bend plane: $\phi = \pm\pi/2$. $S_y = 0.99$ (1% depolarization) corresponds to a distance to the resonance $\Delta = 7|\epsilon_R|$, and spin precession axis at an angle $\phi = \text{acos}(0.99) = 8^o$ from the vertical.

Conversely,

$$\frac{\Delta^2}{|\epsilon_R|^2} = \frac{S_y^2}{1 - S_y^2} \tag{9.43}$$

The precession axis is common to all spins, S_y is a measure of the polarization along the vertical axis,

$$S_y = \frac{N^+ - N^-}{N^+ + N^-}$$

wherein N^+ and N^- denote the number of particles in spin states $\frac{1}{2}$ and $-\frac{1}{2}$ respectively.

Spin motion through weak resonances

Depolarizing resonances are weak up to several GeV in a weak focusing synchrotron, as the radial and/or longitudinal fields, which stem from a small radial field index and from dipole fringe fields, are weak. Spin motion $S_y(\theta)$ through a resonance in that case (*i.e.*, assuming $S_{y,f} \approx S_{y,i}$, with $S_{y,f}$ and $S_{y,i}$ the asymptotic vertical spin component values respectively upstream and downstream of the resonance) can be calculated in terms of the Fresnel integrals

$$C(x) = \int_0^x \cos\left(\frac{\pi}{2}t^2\right) dt, \qquad S(x) = \int_0^x \sin\left(\frac{\pi}{2}t^2\right) dt$$

namely, with the origin of the orbital angle taken at the resonance [22] (Fig. 9.17)

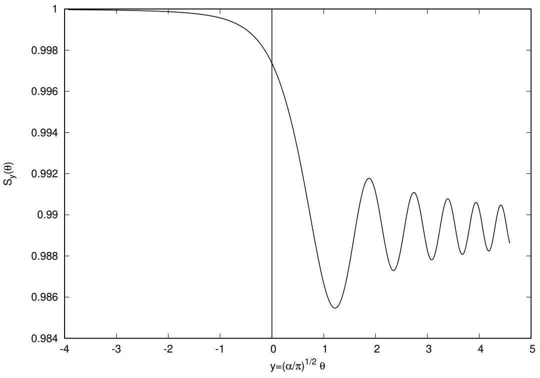

Fig. 9.17 Vertical component of spin motion $S_y(\theta)$ through a weak depolarizing resonance (after Eq. 9.44). The vertical bar is at the location of the resonance, which coincides with the origin of the orbital angle

$$\begin{aligned} if\ \theta < 0: \ \left(\frac{S_y(\theta)}{S_{y,i}}\right)^2 &= 1 - \frac{\pi}{\alpha}|\epsilon_R|^2 \left\{\left[0.5 - C\left(-\theta\sqrt{\frac{\alpha}{\pi}}\right)\right]^2 + \left[0.5 - S\left(-\theta\sqrt{\frac{\alpha}{\pi}}\right)\right]^2\right\} \\ if\ \theta > 0: \ \left(\frac{S_y(\theta)}{S_{y,i}}\right)^2 &= 1 - \frac{\pi}{\alpha}|\epsilon_R|^2 \left\{\left[0.5 + C\left(\theta\sqrt{\frac{\alpha}{\pi}}\right)\right]^2 + \left[0.5 + S\left(\theta\sqrt{\frac{\alpha}{\pi}}\right)\right]^2\right\} \end{aligned} \tag{9.44}$$

In the asymptotic limit,

$$\frac{S_y(\theta)}{S_{y,i}} \xrightarrow{\theta\to\infty} 1 - \frac{\pi}{\alpha}|\epsilon_R|^2 \tag{9.45}$$

which identifies with the development of Froissart-Stora formula $P_f/P_i = 2\exp(-\frac{\pi}{2}\frac{|\epsilon_R|^2}{\alpha})-1$, to first order in $|\epsilon_R|^2/\alpha$. This approximation holds in the limit that higher order terms can be neglected, *viz.* $|\epsilon_R|^2/\alpha \ll 1$.

9.2 Exercises

9.1 Construct Saturne I synchrotron. Spin Resonances

Solution: page 324

In this exercise, Saturne I synchrotron is modeled in `zgoubi`, and spin resonances in a weak focusing gradient synchrotron are studied.

(a) Construct a model of Saturne I 90^o cell dipole in the hard-edge model, using DIPOLE. Use parameters given in Tab. 9.1, and Fig. 9.18 as a guidance. Take an integration step size in centimeter range - check convergence as you proceed. In order to allow beam monitoring, split the dipole in two 45^odeg halves. It is judicious (although in no way a necessity) to take RM=841.93 cm in DIPOLE.

Find the 6×6 transport matrix of that dipole. MATRIX can be used for that, with OBJET[KOBJ=5] to define a proper set of initial coordinates.

Check against theory (refer to Sect. 18.2, Eq. 18.31).

(b) Construct a model of Saturne I cell, with origin at the center of the drift. Take the reference orbit along the arc of nominal radius in the dipoles, 841.93 cm.

Compute the tunes using MATRIX; check their values against theory.

Move the origin along the drift, verify that, while the cell matrix depends on the origin, its trace does not change.

Produce a scan of the tunes over the field index range $0.5 \leq n \leq 0.757$. REBELOTE can be used to repeatedly change n over that range. Superimpose the theoretical curves $\nu_x(n)$, $\nu_y(n)$.

Using TWISS and OBJET[KOBJ=5], produce the periodic beam matrix of the cell. TWISS causes a print out of both the transport matrix and the periodic beam matrix: check that these satisfy Eq. 19.14.

(c) Launch 60 particles evenly distributed on a common paraxial horizontal Courant-Snyder invariant (vertical motion is taken null). Store particle data along the ring in zgoubi.plt, using DIPOLE[IL=2] and DRIFT[split,N=20,IL=2]. Use these to produce a graph of $x^2(s)\ /\ \varepsilon_x/\pi$.

From this graph, get the value of the betatron function β_x at the ends of the cell, compare with TWISS outcomes. Find the minimum and maximum values of the beta functions, and their azimuth $s(min[\beta_x])$, $s(max[\beta_x])$. Check the latter against theory.

Repeat for the vertical motion, taking $\varepsilon_x = 0$, ε_y paraxial.

(d) Answer the previous question using, instead of 60 particles, a single particle traced over a few tens of turns.

(e) Find the closed orbit for an off-momentum particle. FIT can be used for that. From the raytracing outcomes, produce a graph of the dispersion function $D_x(s)$.

(f) Justify considering the betatron oscillation as sinusoidal, namely,

$$y(\theta) = A\ \cos(\nu_y\theta + \phi)$$

wherein $\theta = s/R$, $R = \oint ds/2\pi$.

Find the value of the horizontal and vertical betatron functions, resulting from that approximation. Compare with the betatron functions obtained in (b).

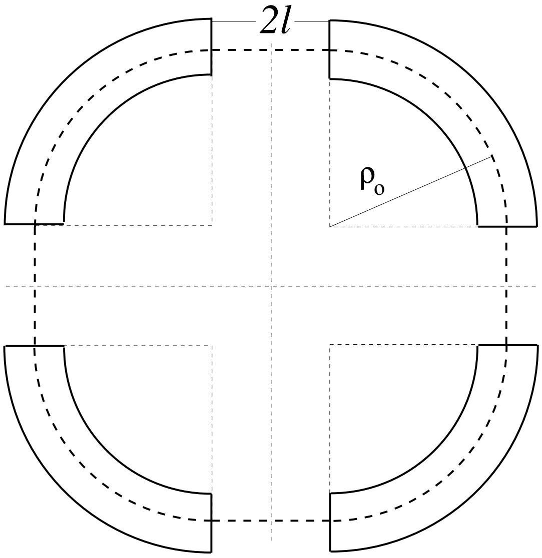

Fig. 9.18 A schematic layout of Saturne I, a $2\pi/4$ axial symmetry structure, comprised of 4 radial field index 90 deg dipoles and 4 drift spaces. The cell in the simulation exercises is taken as a $\pi/4$ quadrant: l-drift/90^o-dipole/l-drift

Table 9.1 Parameters of Saturne 1 weak focusing synchrotron [23]. ρ_0 denotes the reference bending radius in the dipole; the reference orbit, field index, wave numbers, etc., are taken along that radius

Orbit length, C	cm	6890
Average radius, $R = C/2\pi$	cm	1096.58
Straight section length. $2l$	cm	400
Magnetic radius, ρ_0	cm	841.93
R/ρ_0		1.30246
Field index n, nominal value		0.6
Wave numbers, ν_x; ν_y		0.724; 0.889
Stability limit		$0.5 < n < 0.757$
Injection energy	MeV	3.6
Field at injection	kG	0.0326
Top energy	GeV	2.94
$\dot{B}$	T/s	1.8
Field at top energy, $B_{\max}$	kG	14.9
$B_{\max}\rho$	T m	13
Field ramp at injection	kG/s	20
Synchronous energy gain	keV/turn	1.160
RF harmonic		2

(g) Produce an acceleration cycle from 3.6 MeV to 3 GeV, for a few particles launched on a common $10^{-4}\,\pi$m initial invariant in each plane. Ignore synchrotron motion (CAVITE[IOPT=3] can be used in that case). Take a peak voltage $\hat{V} = 200$ kV (unrealistic though, as it would result in a nonphysical $\dot{B}$ (Eq. 9.30)) and synchronous phase $\phi_s = 150$ deg (justify $\phi_s > \pi/2$).

Check the accuracy of the betatron damping over the acceleration range, compared to theory.

How close to symplectic the numerical integration is (it is by definition *not* symplectic, being a truncated Taylor series method [24, Eq. 1.2.4]), depends on the integration step size, and on the size of the flying mesh in the DIPOLE method [24, Fig. 20]; check a possible departure of the betatron damping from theory as a function of these parameters.

Produce a graph of the the evolution of the horizontal and vertical wave numbers during the acceleration cycle.

(h) Change the peak voltage to $\hat{V} = 20\,\mathrm{kV}$. Produce a graph of the value of the vertical spin component of the particles as a function of $G\gamma$, over the acceleration range from 3.6 MeV to 3 GeV. Adding SPNTRK will ensure spin tracking.

Produce a graph of the average value of S_Z over that 200 particle set, as a function of $G\gamma$. Indicate on that graph the location of the resonant $G\gamma_R$ values.

(i) Based on the simulation file used in (f), simulate the acceleration of a single particle, through the intrinsic resonance $G\gamma_R = 4 - \nu_Z$, from a few thousand turns upstream to a few thousand turns downstream.

Perform this resonance crossing for five different values of the particle invariant, namely: $\varepsilon_Z/\pi = 2,\ 10,\ 20,\ 40,\ 200\,\mu\mathrm{m}$.

Compute P_f/P_i in each case, check the dependence on ε_Z against theory. Compute the resonance strength in each case, check the dependence on ε_Z against theory.

Re-do this crossing simulation for a different crossing speed (take for instance $\hat{V} = 10\,\mathrm{kV}$) and a couple of vertical invariant values, compute P_f/P_i so obtained. Check the crossing speed dependence of P_f/P_i against theory.

(j) Plot the turn-by-turn vertical spin component motion $S_Z(turn)$ across the resonance $G\gamma_R = 4 - \nu_Z$, in a weakly depolarizing case, $P_f \approx P_i$. Show that it satisfies Eq. 9.44. Match the data to the latter to get the vertical betatron tune ν_y, and the location of the resonance $G\gamma_\mathrm{R}$.

(k) Track a few particles at fixed energy, at distances from the resonance $G\gamma_R = 4 - \nu_y$ of up to a $7 \times \epsilon_R$ (this distance corresponds to 1% depolarization).

Produce on a common graph the spin motion $S_Z(turn)$ for all these particles, as observed at some azimuth along the ring.

Produce a graph of $\langle S_y \rangle|_\mathrm{turn}(\Delta)$ (as in Fig. 9.16).

Produce the vertical betatron tune ν_y, and the location of the resonance $G\gamma_\mathrm{R}$, obtained from a match of these tracking trials to the theoretical (Eq. 9.42)

$$\langle S_y \rangle (\Delta) = \frac{\Delta}{\sqrt{|\epsilon_R|^2 + \Delta^2}}$$

9.2 Construct the ZGS synchrotron. Spin Resonances

Solution: page 347

In this exercise, ZGS synchrotron is modeled in `zgoubi`, and spin resonances in this weak focusing zero-gradient synchrotron are studied.

(a) Construct an approximate model of the ZGS synchrotron, using DIPOLE. Use Figs. 9.19, 9.20 as a guidance, and parameters given in Tab. 9.2. Assume that the reference orbit is the same at all energies, on nominal radius, 2076 cm. It is judicious (although in no way an obligation) to take RM=2076 in DIPOLE. (Note that in reality, unlike the present assumption for this exercise, the reference orbit in ZGS would be moved outward during acceleration [25].)

Check the correctness of the model by producing the lattice parameters of the ring. TWISS can be used for that. Compare with the lattice parameters given in Tab. 9.2.

(b) Produce a graph of the betatron functions along the ZGS cell. Provide checks of the correctness of the computation.

Check the theoretical periodic dispersion (Eq. 9.27) against the radial distance between on- and off-momentum closed orbits obtained from raytracing. Provide a plot of the dispersion function.

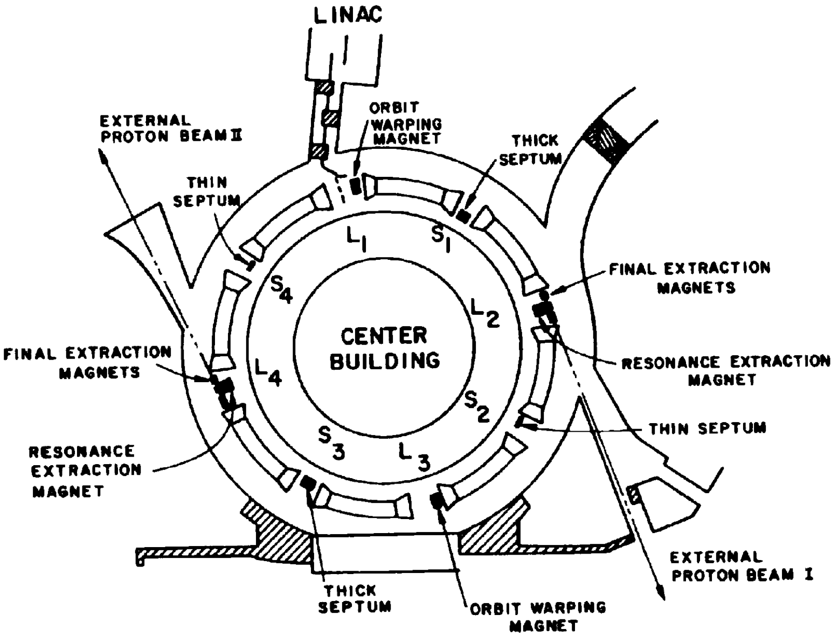

Fig. 9.19 A schematic layout of the ZGS [**?**], a $\pi/2$-periodic structure, comprised of 8 zero-index dipoles, 4 long and 4 short straight sections

(c) Additional verifications regarding the model.

Produce a graph of the field B(s)

- along the on-momentum closed orbit, and along off-momentum chromatic closed orbits, across a cell;
- along orbits at large horizontal excursion;
- along orbits at large vertical excursion.

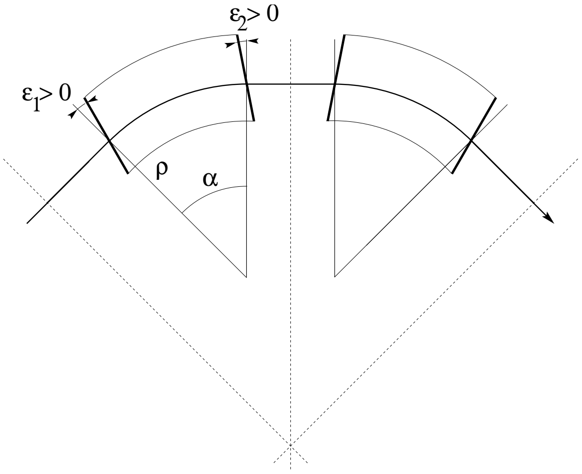

Fig. 9.20 A sketch of ZGS cell layout. In defining the entrance and exit faces (EFBs) of the magnet, beam goes from left to right. Wedge angles at the long straight sections (ε_1) and at the short straight sections (ε_2) are different

For all these cases, verify qualitatively, from the graphs, that $B(s)$ appears as expected.

(d) Justify considering the betatron oscillation as sinusoidal, namely,

$$y(\theta) = A\,\cos(\nu_y\theta + \phi)$$

wherein $\theta = s/R$, $R = \oint ds/2\pi$.

Find the value of the horizontal and vertical betatron functions, resulting from that approximation. Compare with the betatron functions obtained in (b).

(e) Produce an acceleration cycle from 50 MeV to 17 GeV about, for a few particles launched on the a common $10^{-5}\,\pi$m vertical initial invariant, with small horizontal invariant. Ignore synchrotron motion (CAVITE[IOPT=3] can be used in that case). Take a peak voltage $\hat{V} = 200\,$kV (this is unrealistic but yields 10 times faster computing than the actual $\hat{V} = 20\,$kV, Tab. 9.2) and synchronous phase $\phi_s = 150\,$deg (justify $\phi_s > \pi/2$). Add spin, using SPNTRK, in view of the next question, (f).

Check the accuracy of the betatron damping over the acceleration range, compared to theory. How close to symplectic the numerical integration is (it is by definition *not* symplectic), depends on the integration step size, and on the size of the flying mesh in the DIPOLE method [24, Fig. 20]; check a possible departure of the betatron damping from theory as a function of these parameters.

Produce a graph of the the evolution of the horizontal and vertical wave numbers during the acceleration cycle.

Table 9.2 Parameters of the ZGS weak focusing synchrotron after Refs. [25, 26] [**?**, pp. 288-294,p. 716] (2nd column, when they are known) and in the present simplified model and numerical simulations (3rd column). Note that the actual orbit is skewed (moves) during ZGS acceleration cycle, tunes change as well - this is not the case in the present modeling

		From Refs. [25, 26]	**Simplified model**
Injection energy	MeV	50	
Top energy	GeV	12.5	
$G\gamma$ span		1.888387 - 25.67781	
Length of central orbit	m	171.8	170.90457
Length of straight sections, total	m	41.45	40.44
Lattice			
Wave numbers ν_x; ν_y		0.82; 0.79	0.849; 0.771
Max. β_x; β_y	m		32.5; 37.1
Magnet			
Length	m	16.3	16.30486 (magnetic)
Magnetic radius	m	21.716	20.76
Field min.; max.	kG	0.482; 21.5	0.4986; 21.54
Field index		0	
Yoke angular extent	deg	43.02590	45
Wedge angle	deg	≈10	13 and 8
RF			
Rev. frequency	MHz	0.55 - 1.75	0.551 - 1.751
RF harmonic h=$\omega_{\mathrm{rf}}/\omega_{\mathrm{rev}}$		8	
Peak voltage	kV	20	200
B-dot, nominal/max.	T/s	2.15/2.6	
Energy gain, nominal/max.	keV/turn	8.3/10	100
Synchronous phase, nominal	deg	150	
Beam			
ε_x; ε_y (at injection)	$\pi\mu$m	25; 150	
Momentum spread, rms		3×10^{-4}	
Polarization at injection	%	>75	100
Radial width of beam (90%), at inj.	inch	2.5	$\sqrt{\beta_x \varepsilon_x/\pi} = 1.1$

(f) Using the raytracing material developed in (e): produce a graph of the vertical spin component of the particles, and the average value over that 200 particle set, as a function of $G\gamma$. Indicate on that graph the location of the resonant $G\gamma_R$ values.

(g) Based on the simulation file used in (f), simulate the acceleration of a single particle, through one particular intrinsic resonance, from a few thousand turns upstream to a few thousand turns downstream.

Perform this resonance crossing for different values of the particle invariant. Determine the dependence of final/initial vertical spin component value, on the invariant value; check against theory.

Re-do this crossing simulation for a different crossing speed. Check the crossing speed dependence of final/initial vertical spin component so obtained, against theory.

(h) Introduce a vertical orbit defect in the ZGS ring.

Find the closed orbit.

Accelerate a particle launched on that closed orbit, from 50 MeV to 17 GeV about, produce a graph of the vertical spin component.

Select one particular resonance, reproduce the two methods of (g) to check the location of the resonance at $G\gamma_R$ =integer, and to find its strength.

References

1. Veksler, V.: A new method of acceleration of relativistic particles. J. of Phys. USSR 9 153-158 (1945)
2. McMillan, E. M.: The Synchrotron. Phys. Rev. 68 143-144 (1945)
3. Goward, F. K., and Barnes, D. E.: Experimental 8 MeV synchrotron for electron acceleration. Nature 158, 413 (1946)
4. Richardson, J.R., et al.: Frequency Modulated Cyclotron. Phys. Rev. 69: 669 (1946)
5. Kerst, D. W.: The Acceleration of Electrons by Magnetic Induction.. Phys. Rev., 60, 47-53 (1941)
6. Photo saturne I. ********* TB completed **** Archives historiques CEA. Copyright CEA/Service de documentation - FAR_SA_N_00248
7. Photo tranche dipole. Credit: CEA Saclay. *********** TB completed *********** Archives historiques CEA. Copyright CEA/Service de documentation - FAR_SA_N_02826
8. Photo synch ring loma linda *********** TB completed *********** synchWF_copyRights_Saturne
9. Ratner, L.G. and Khoe, T.K.: Acceleration of Polarized Protons in the Zero Gradient Synchrotron. Procs. PAC 1973 Conference, Washington (1973). http://accelconf.web.cern.ch/p73/PDF/PAC1973_0217.PDF
10. Endo, K., et al.: Compact proton and carbon ion synchrotrons for radiation therapy. MOPRI087, Proceedings of EPAC 2002, Paris, France; pp. 2733-2735. https://accelconf.web.cern.ch/e02/PAPERS/MOPRI087.pdf
11. Vostrikov, V.A., et al.: Novel approach to design of the compact proton synchrotron magnetic lattice. tupsa17, 26th Russian Particle Accelerator Conference RUPAC2018, Protvino, Russia (2018). https://accelconf.web.cern.ch/rupac2018/papers/tupsa17.pdf
12. Suddeth, D.E., et als.: Pole face winding equipment for eddy current correction at the Zero Gradient Synchrotron. Procs. PAC 1973 Conference, Washington (1973). http://accelconf.web.cern.ch/p73/PDF/PAC1973_0397.PDF
13. Rauchas, A.V. and Wright, A.J.: Betatron tune profile control in the Zero Gradient Synchrotron (ZGS) using the main magnet pole face windings. Procs. PAC1977 conference, IEEE Trans. on Nucl. Science, VoL.NS-24, No.3, June 1977

14. Floquet, G.: Sur les équations différentielles linéaires à coefficients périodiques. Annales scientifiques de l'E.N.S. 2e série, tome 12 (1883), p. 47-88. http://www.numdam.org/item?id=ASENS_1883_2_12__47_0
15. Leleux, G.: Accélérateurs Circulaires. Lecture Notes, INSTN, CEA Saclay (1978)
16. Bohm, D. and Foldy, L.: Theory of the Synchro-Cyclotron. Phy. Rev. 72, 649-661 (1947).
17. Cohen, D, : Feasibility of Accelerating Polarized Protons with the Argonne ZGS. Review of Scientific Instruments 33, 161 (1962).// https://doi.org/10.1063/1.1746524
18. Cho, Y., et als.: Effects of depolarizing resonances on a circulating beam of polarized protons during or storage in a synchrotron. IEEE Trans. Nuclear Science, Vol.NS-24, No.3, June 1977
19. Parker, E.F.: High Energy Polarized Deuterons at the Argonne National Laboratory Zero Gradient Synchrotron. IEEE Transactions on Nuclear Science, Vol. NS-26, No. 3, June 1979, pp 3200-3202
20. Lee, S.Y.: Spin Dynamics and Snakes in Synchrotrons. World Scientific, 1997
21. Froissart, M. and Stora, R.: Dépolarisation d'un faisceau de protons polarisés dans un synchrotron. Nucl. lnst. Meth. 7 (l960) 297.
22. Leleux, G.: Traversée des résonances de dépolarisation. Rapport Interne LNS/GT-91-15, Saturne, Groupe Théorie, CEA Saclay (février 1991)
23. Bruck H., Debraine P., Levy-Mandel R., Lutz J., Podliasky I., Prevot F., Taieb J., Winter S.D., Maillet R., Caractéristiques principales du Synchrotron à Protons de Saclay et résultats obtenus lors de la mise en route, rapport CEA no.93, CEN-Saclay, 1958.
24. Méot, F.: Zgoubi Users' Guide. https://www.osti.gov/biblio/1062013-zgoubi-users-guide Sourceforge latest version: https://sourceforge.net/p/zgoubi/code/HEAD/tree/trunk/guide/Zgoubi.pdf
25. Foss, M.H., et al.: The Argonne ZGS Magnet. IEEE 1965, pp. 377-382, June 1965
26. Klaisner, L.A., et al.: IEEE 1965, pp. 133-137, June 1965